

## On the wake flow of asymmetrically beveled trailing edges

Guan, Yaoyi; Pröbsting, Stefan; Stephens, David; Gupta, A.; Morris, Scott C.

**DOI**

[10.1007/s00348-016-2172-2](https://doi.org/10.1007/s00348-016-2172-2)

**Publication date**

2016

**Document Version**

Accepted author manuscript

**Published in**

Experiments in Fluids: experimental methods and their applications to fluid flow

**Citation (APA)**

Guan, Y., Pröbsting, S., Stephens, D., Gupta, A., & Morris, S. C. (2016). On the wake flow of asymmetrically beveled trailing edges. *Experiments in Fluids: experimental methods and their applications to fluid flow*, 57(5), Article 78. <https://doi.org/10.1007/s00348-016-2172-2>

**Important note**

To cite this publication, please use the final published version (if applicable). Please check the document version above.

**Copyright**

Other than for strictly personal use, it is not permitted to download, forward or distribute the text or part of it, without the consent of the author(s) and/or copyright holder(s), unless the work is under an open content license such as Creative Commons.

**Takedown policy**

Please contact us and provide details if you believe this document breaches copyrights. We will remove access to the work immediately and investigate your claim.

# On the Wake Flow of Asymmetrically Beveled Trailing Edges

Yaoyi Guan · Stefan Pröbsting · David  
Stephens · Abhineet Gupta · Scott C.  
Morris

Received: date / Accepted: date

**Abstract** Trailing edge and wake flows are of interest for a wide range of applications. Small changes in the design of asymmetrically beveled or semi-rounded trailing edges can result in significant difference in flow features which are relevant for the aerodynamic performance, flow-induced structural vibration and aerodynamically generated sound. The present study describes in detail the flow field characteristics around a family of asymmetrically beveled trailing edges with an enclosed trailing-edge angle of  $25^\circ$  and variable radius of curvature  $R$ .

The flow fields over the beveled trailing edges are described using data obtained by Particle Image Velocimetry (PIV) experiments. The flow topology for different trailing edges was found to be strongly dependent on the radius of curvature  $R$ , with flow separation occurring further downstream as  $R$  increases. This variation in the location of flow separation influences the aerodynamic force coefficients, which were evaluated from the PIV data using a control volume approach. Two-point correlations of the in-plane velocity components are considered to assess the structure in the flow field. The analysis shows large-scale coherent motions in the far wake, which are associated with vortex

---

Y. Guan

Department of Aerospace and Mechanical Engineering, University of Notre Dame  
E-mail: yguan@nd.edu

S. Pröbsting

Department of Aerodynamics, Wind Energy, Flight Performance and Propulsion, Delft University of Technology

D. Stephens

Glenn Research Center, NASA

A. Gupta

Department of Aerodynamics, Wind Energy, Flight Performance and Propulsion, Delft University of Technology

S. C. Morris

Department of Aerospace and Mechanical Engineering, University of Notre Dame

shedding. The wake thickness parameter  $y_f$  is confirmed as an appropriate length scale to characterize this large-scale roll-up motion in the wake. The development in the very near wake was found to be critically dependent on  $R$ . In addition, high-speed PIV measurements provide insight into the spectral characteristics of the turbulent fluctuations. Based on the time-resolved flow field data, the frequency range associated with the shedding of coherent vortex pairs in the wake is identified. By means of time-correlation of the velocity components, turbulent structures are found to convect from the attached or separated shear layers without distinct separation point into the wake.

**Keywords** First keyword · Second keyword · More

## 1 Introduction

The flow over the trailing edge of an airfoil is an important topic that affects many aspects of engineering design. For instance, the lift and drag characteristics of an airfoil are highly sensitive to the trailing-edge shape. A sharper trailing edge will generally provide superior aerodynamic characteristics [Blake, 1986]. However, scattering of turbulent pressure fluctuations from the sharp edge leads to efficient production of radiated sound [Amiet, 1976]. This mechanism of sound generation often dominates at higher frequency ( $fc/a_o \gg 1$ , where  $f$  is frequency,  $c$  is chord length,  $a_o$  is acoustic speed), particularly in turbomachinery applications (e.g. fans, propellers, wind turbines) [Blake, 1986, Roger and Moreau, 2004]. Unsteady surface pressure fluctuations can also lead to structural vibration and material fatigue under long term exposure. Hence, first considerations related to sound and vibration can motivate thicker, blunt trailing edge shapes. On the downside, this design choice can lead to strong and coherent vortex shedding, which may cause additional and potentially even more severe sound and vibration issues. Design of trailing edges for low sound and vibration while maintaining aerodynamic performance therefore requires understanding of the flow field in the wake, as well as identification of the relevant parameters that influence its characteristics.

Sound radiation from trailing edges has been treated analytically in the works of Ffowcs Ffowcs Williams and Hall [1970], Howe [1975, 1976], Amiet [1976], Blake [1986], and others. On the experimental side, a large number of studies have been reported since the identification of edge noise as one of the dominant airfoil self-noise mechanisms in low Mach number flow. For instance, Olsen and Boldman [1979] utilized a horizontal, circular array of condenser microphones to measure the radiated sound generated by various trailing edges and the corresponding flow pattern was determined by hot-wire measurements. Schlinker [1977] measured the trailing-edge noise generated by NACA 0012 and NACA 0018 airfoil profiles using highly directional microphone systems in order to reduce the contribution of parasitic (unwanted) noise sources. He noted that the sound radiated from the trailing edges of symmetric airfoils is strongly affected by the development of the turbulent

boundary layer. Brooks and Hodgson [1981] conducted extensive surface pressure and acoustic measurements and described an experimental methodology for noise prediction from the statistics of the measured unsteady surface pressure. Later, Devenport et al. [2001] measured two-point correlations of the velocity field in the near wake of a NACA 0012 airfoil employing hot-wire anemometry. Although the data provided valuable information regarding the spatial and temporal scales of the wake flow, the correlation approach does not facilitate a detailed understanding of the noise generation mechanism and underlying flow dynamics. Moreover, hot-wires are not well-suited for blunt trailing-edge flows where the near wake flow is separated and recirculating. More recently, Shannon and Morris [2006] and Nakano et al. [2006] utilized phase-averaged PIV to describe the flow field around a trailing edge. Utilizing time-resolved PIV, Pröbsting et al. [2014b] experimentally described the boundary layer flow over a NACA 0012 generating tonal noise. Downstream convecting vortical structures were found to coherently pass the trailing edge at a frequency equal to that of the dominant tone. Recently, Pröbsting et al. [2015] described a methodology for the prediction of broadband noise radiation due to the interaction of the turbulent boundary layer with the trailing edge based on the reconstructed pressure field based on high-speed tomographic PIV measurements. Due to the information it provides in both space and time, high-speed PIV constitutes an excellent tool for the study of the aeroacoustic source field, in particular in the confined region around trailing edges [Morris, 2011].

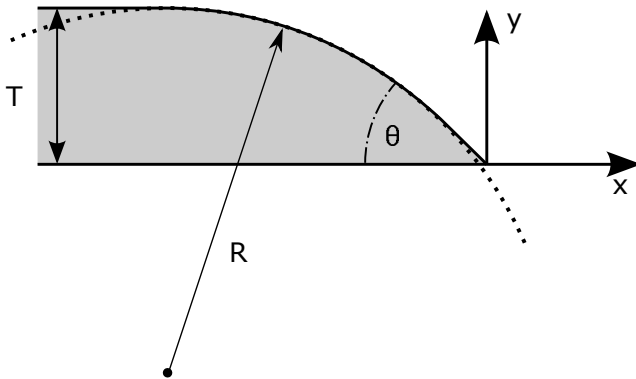


**Fig. 1** Parametric representation of beveled trailing edge.

In an attempt to systematically study trailing edge flows for flat struts, Blake and co-workers [Blake, 1975, 1984, Gershfeld et al., 1988] introduced a class of semi-rounded (also: asymmetrically beveled) trailing edges. The members of this class can be characterized by an angle  $\theta$ , which is enclosed between the surfaces at the trailing edge, and the ratio of radius of curvature of the rounded part  $R$  over the plate thickness  $T$  (Figure 1).  $R/T = 0$  results in an obtuse corner on the upper surface. For  $R/T > 0$ , an arc with the re-

spective radius of curvature is tangent to both the upper, horizontal surface and the inclined surface at the trailing edge. Generally, the details of the flow field depend on the geometry ( $\theta$ ,  $R/T$ ) and on the flow conditions, given by Reynolds number ( $\text{Re} = u_\infty T/\nu$ , where  $\nu$  is the kinematic viscosity) and the bluntness parameter ( $T/\delta^*$ , where  $\delta^*$  is the boundary layer displacement thickness). Larger radii of curvature ( $R/T$ ) and Reynolds numbers ( $\text{Re}$ ) result in delayed separation on the upper surface towards the trailing edge. Conversely, for larger values of  $\theta$  a larger region of separated and reverse flow is expected [Blake, 1986]. Since the introduction of this geometry, it has served as test case for sound and vibration studies on trailing edges due to the variety of flow conditions that can be reproduced, including mildly adverse pressure gradients and large-scale separation. Most of these works focused on families with comparatively blunt ( $\theta = 45^\circ$ ) and sharp ( $25^\circ$ ) trailing edges, which show marked differences in flow structure and related noise emission as pointed out by Blake [1984]. Specifically trailing edges with  $\theta > 30^\circ$  are likely to produce vortex shedding due to separation and thus tonal noise, while for sharper edges noise is primarily of broadband nature.

The case with  $\theta = 45^\circ$  ( $R/T = 2.5$ ) was first investigated by Blake [1975] in a series of well-defined experiments on the unsteady flows around squared-off and asymmetrically beveled trailing edges. He reported strong vortex shedding in the wake and introduced a set of scaling parameters used to describe the flow structure, namely the wake thickness parameter  $y_f$  and the velocity  $U_s$  along the so-called free streamline at separation, which was defined by Roshko [1954]. With these scaling parameters, the dimensionless angular shedding frequency was found to be close to unity at  $\omega_s y_f / u_s \approx 1$  ( $\omega = 2\pi f$ , with  $f$  the ordinary frequency). In an early numerical study, Knight and Peltier [1997] simulated the flow around a  $45^\circ$  trailing edge similar to the one used in Blake's experiments [Blake, 1975] by an unsteady, two-dimensional Reynolds-averaged Navier-Stokes (RANS) method. The predicted shedding frequency was consistent with the experimental results, while a good qualitative agreement was found for pressure-velocity correlations and turbulence intensity. Later, Manoha et al. [2000] performed a Large-Eddy Simulation (LES) of the incompressible flow around the blunt trailing edge of a thick plate. While the shedding frequency was in good agreement with the results of Blake [1975], the solution showed vortex shedding with a three-dimensional instability mechanism, which could not be captured in earlier simulations. Wang [2005] utilized a similar LES approach to simulate the flow field and related acoustic sources to predict the radiated sound from a  $45^\circ$  ( $R/T = 2.5$ ) trailing edge. The solution was validated against the experimental measurements of Olson and Mueller [2004]. Also in this case, large and spanwise coherent vortices in the wake were found to shed into the wake. In order to analyze the shedding process in greater detail, Shannon and Morris [2006] employed planar, low-repetition-rate PIV measurements in the wake of a similar  $45^\circ$  trailing edge and used the results to describe the phase-averaged shedding cycle. They reported asymmetric periodic vortex shedding to occur at a constant shedding frequency  $\omega_s y_f / u_\infty = 1.15$ , where  $u_\infty$  is the free stream velocity. The authors described

the character of the small-scale turbulence in the vicinity of the sharp trailing edge to be dependent on the phase of the large-scale vortex-shedding motion.

Sharper beveled trailing edges with an enclosed angle of  $\theta = 25^\circ$  were studied extensively by Blake [Blake, 1975, 1984, 1986]. In comparison to the case with  $\theta = 45^\circ$  discussed above, such geometries do not generally exhibit pronounced vortex shedding and tonal noise. Wang and Moin [2000] utilized an LES method to compute the flow around a similar  $25^\circ$  ( $R/T = 4$ ) edge and did not observe coherent vortex shedding. Instead, on a statistical basis the authors reported an increase in the time scales and spanwise correlation over the separated flow region. Kunze et al. [2002] presented preliminary acoustic measurements of two geometries including a beveled edge with an enclosed angle of  $\theta = 30^\circ$ . They found a knuckle-beveled trailing edge ( $R/T = 0$ ) to generate tonal noise resulting due to vortex shedding while the rounded-beveled edge ( $R/T = 4$ ) exhibited primarily broadband noise. Related to the present work, Pröbsting et al. [2014a] presented the flow field and radiated sound of a  $25^\circ$  beveled trailing edge with large radius of curvature ( $R/T = 10$ ) using high-speed and tomographic PIV. At such large radius of curvature, the boundary layer remains attached up to the trailing edge and the results showed small-scale vortical structures with comparatively low convective velocity close to the surface in the adverse pressure gradient flow.

Despite the large number of previous studies on beveled trailing edges, questions with regard to the influence of the main geometric parameters ( $\theta$ ,  $R/T$ ) remain open since the majority of the studies cited above focused on a single geometry or on a small subset thereof. However, comparison of these results suggests that small changes in geometry can have a large effect on important flow features related to the size and coherence of the wake. This holds in particular for the the radius of curvature  $R/T$ . To identify and characterize the effect of small changes in geometry, the present study is set to describe in detail the wake flow for a large family of  $25^\circ$  trailing edges with radii of curvature  $0 \leq R/T \leq 10$ . This family of trailing edges allows for a systematic study of flow fields with conditions ranging from separated flows with large scale unsteady vortex shedding to fully attached, adverse pressure gradient boundary layers and near-steady wakes. By changing the curvature of the upper surface, the extents of the adverse pressure gradient and separated flow regions likewise change. A detailed flow field description is obtained by planar, two-component, statistical and time-resolved PIV measurements. The mean flow topology, turbulence characteristics, and correlations of the velocity fluctuations in the shear layers are discussed and related to the results reported in literature.

## 2 Experimental setup and methods

### 2.1 Airfoil geometry and boundary conditions

The airfoil models were constructed as a flat strut with a uniform cross section across the span, similar to the ones used in previous studies [Blake, 1975, 1984] with a maximum thickness of  $T/c = 5.6\%$  relative to the chord  $c$ . The cross section of the leading edge component of the airfoil was a five-to-one aspect ratio semi-ellipse. The trailing-edge component was exchangeable and the different geometries utilized are described in the following. To ensure a turbulent boundary layer flow upstream of the trailing edge, transition was forced at a location quarter chord downstream of the leading edge ( $x/c = -0.75$ ) on both sides of the airfoil. The plate was fixed at zero incidence for all experiments.

The measurement program was divided into two separate measurement campaigns. A first part was conducted on large-scale models using low-repetition-rate PIV for a large field-of-view (FOV) at the University of Notre Dame. Here, the chord, thickness, and span of the model was  $c = 914\text{mm}$ ,  $T = 50.8\text{mm}$ , and  $L = 610\text{mm}$ , respectively, and the tests were conducted at Reynolds number  $\text{Re} = 1.1 \times 10^6$  (free-stream reference velocity  $u_\infty \approx 20\text{m/s}$ , measured on the lower side at the location of the trailing edge). The tripping devices consisted of randomly distributed 3D roughness elements (sand grain, nominal size  $290\mu\text{m}$ ) over a width of  $25\text{mm}$ , resulting in a boundary layer thickness  $\delta = 8.6\text{mm}$  and displacement thickness  $\delta^* = 1.2\text{mm}$  for the turbulent boundary layer at  $x/T = -5.5$  (bluntness parameters  $T/\delta = 5.9$  and  $T/\delta^* = 42.3$ ) at a Reynolds number of  $\text{Re} = 1.1 \times 10^6$ . Figure 2 shows the family of asymmetrically beveled trailing edges chosen, consisting of seven geometries with  $\theta = 25^\circ$  with  $0 \leq R/T \leq 10$ .

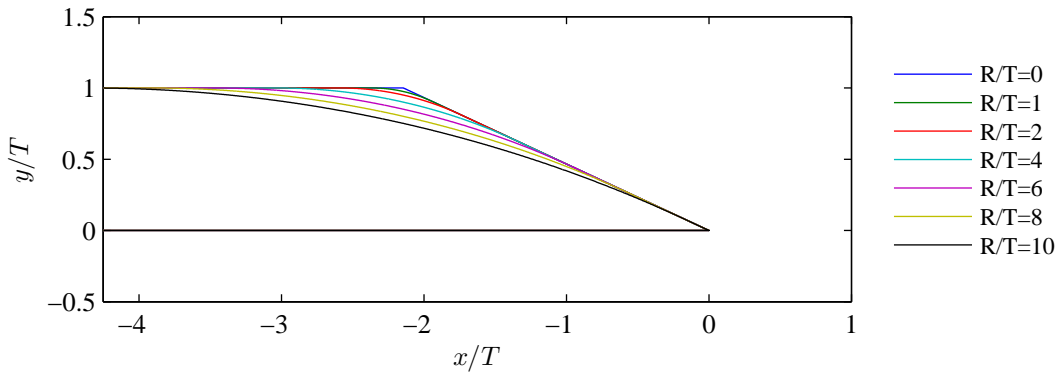


**Fig. 2** The family of  $\theta = 25^\circ$  asymmetrically beveled trailing edge for  $R/T = 0, 1, \dots, 10$ .

**Table 1** Geometric parameters and flow conditions for measurements on large-scale and small-scale models with low-repetition-rate and high-speed PIV, respectively.

parameter	symbol	large-scale models	small-scale models
model chord	$c$	914mm	360mm
model span	$S$	60.96mm	400mm
model thickness	$T$	50.8mm	20mm
trailing edge angle	$\theta$	25°	25°
radius of curvature	$R/T$	0, 1, 2, 4, 6, 8, 10	0, 4, 10
free-stream velocity	$u_\infty$	20m/s	18.4m/s
chord Reynolds number	$Re_c = u_\infty T/\nu$	$1.1 \times 10^6$	$0.42 \times 10^6$
bluntness parameter	$T/\delta$	5.9	3.1
	$T/\delta^*$	42.3	18.2

The second campaign was conducted with high-speed PIV and a smaller field of view (FOV) on the curved part of the upper surface at Delft University of Technology. The models used in these experiments were geometrically similar, but smaller in scale with chord  $c = 360\text{mm}$ , thickness  $T = 20\text{mm}$ , and span  $L = 400\text{mm}$  [Pröbsting et al., 2014a]. Tests were conducted at Reynolds number  $Re = 0.42 \times 10^6$ , corresponding to a free-stream reference velocity of  $u_\infty$  around 18.4m/s. Transition was enforced by randomly distributed 3D roughness elements (nominal size  $840\mu\text{m}$ ) over a width of 10mm, resulting in a boundary layer thickness of  $\delta = 6.5\text{mm}$  and displacement thickness  $\delta^* = 1.1\text{mm}$  for the turbulent boundary layer on the lower surface at  $x/T = -2.5$  (bluntness parameters  $T/\delta = 3.1$  and  $T/\delta^* = 18.2$ ) at a Reynolds number of  $Re = 0.42 \times 10^6$ . A subset of the members of the trailing edge family investigated in the first campaign was selected ( $R/T = 0, 4, 10$ ). Table 1 provides an overview of the relevant parameters related to geometry and flow conditions for the two campaigns.

## 2.2 Facilities and flow field measurements

Figure 3 shows a schematic of the set-up for the PIV measurements on the large-scale models in the 1.83m long closed test section of an open-loop, indraft wind tunnel. A uniform mean velocity ranging from 10 to 33m/s parallel to the test section can be produced by the tunnel with turbulence intensity of 0.4% or less. The cross section of the closed test section was 0.61m by 0.61m and the model was mounted between side plates to ensure spanwise homogeneous flow statistics. A LaVision PIV system with a pair of CCD cameras ( $2048 \times 2048\text{px}$ ,  $7.4\mu\text{m}$  pixel pitch) was used for data collection. The cameras were equipped with Nikon *Micro-Nikkor* 105mm prime lenses. The FOV for each camera is indicated in Figure 3. Illumination was provided by a dual pulsed 120mJ Nd:YAG laser (wavelength 532nm). A light sheet around the trailing edge was formed with a thickness of 1mm through a  $45^\circ$  mirror and beam spreader positioned downstream. A fluorescent paint containing Rhodamine 6G was utilized to coat the surface of the model in order to reduce the reflections from the surface. The synchronization of laser pulses and camera

exposures was controlled by a Programmable Timing Unit. The seeding particles were generated by a Topas ATM 230 aerosol generator which produces droplets of olive oil with diameters ranging from 0.2 to  $1\mu\text{m}$ . The particles were mixed before release into the flow by a particle diffuser consisting of a bank of five small fans, which mixed the particles with the surrounding fluid. The volume flow through the particle diffuser was adjusted such that the outlet velocity of the diffuser was equal to the inlet velocity of the tunnel. This produced a comparatively homogeneous particle distribution in a stream-tube that included only the region of measurement.

1000 image pairs were acquired simultaneously by both cameras at an acquisition frequency of  $f_s = 3\text{Hz}$  and pulse separation  $\Delta t = 100\mu\text{s}$ . The particle displacement was computed using the cross-correlation technique implemented in the software package LaVision DaVis. Prior to correlation, the intensity of the recorded images was normalized. Image cross-correlation was performed with a final interrogation window size of 64px, 75% overlap, and with a two-to-one streamwise-elongated Gaussian window weighting. As predictor, an initial interrogation window shift equivalent to the displacement of the particles in the free stream was applied.

Uncertainty in PIV measurement is influenced by the uniformity of seeding particles, the camera focus, and the illumination of the particles in each interrogation window. Thus, uncertainty can vary over the measurement region and between PIV realizations. An estimate of the uncertainty of PIV measurements for present study can be made assuming a subpixel accuracy of 0.1 pixels (typically reported for planar PIV experiments [Raffel et al., 2007]), which corresponds to a particle displacement accuracy of 0.0143 mm, implying that the velocity measurements have an uncertainty of approximately 0.63% when compared to the free stream velocity. This estimates agrees with the measured root mean square of the velocity in regions where the flow is nominally steady.

High-speed PIV experiments on the small scale models were conducted in an open-jet facility at Delft University of Technology as shown in Figure 4. The wind tunnel has a speed range of about 5 to 35 m/s. There is a straight part after the contraction for straightening the flow. The turbulence level is on the order of 0.5%. The jet had a square nozzle outlet of 0.4m by 0.4m and the airfoil was mounted vertically. At the top and at the bottom of the test section, side plates were mounted flush to the exit nozzle to restrict the expansion of the open jet in the spanwise coordinate direction and avoid 3D flow effects. Two Photron Fastcam SA1.1 (1Mpx, 12bit resolution,  $20\mu\text{m}$  pixel pitch) were used for image acquisition and operated with a reduced active sensor area ( $1024 \times 512\text{px}$ ) for the high-speed acquisition. The cameras were equipped with Nikon Micro-Nikkor 105mm prime lenses and positioned on opposite sides (top and bottom) of the test section with a small offset in the streamwise coordinate direction (Figure 4). The aperture number was set to a  $f\# = 5.6$  to capture sufficient light. At such high aperture the particle images are small, which results in partial peak locking. To reduce this effect, the particle images were slightly defocused [Overmars et al., 2010]. The resulting FOV encompassed

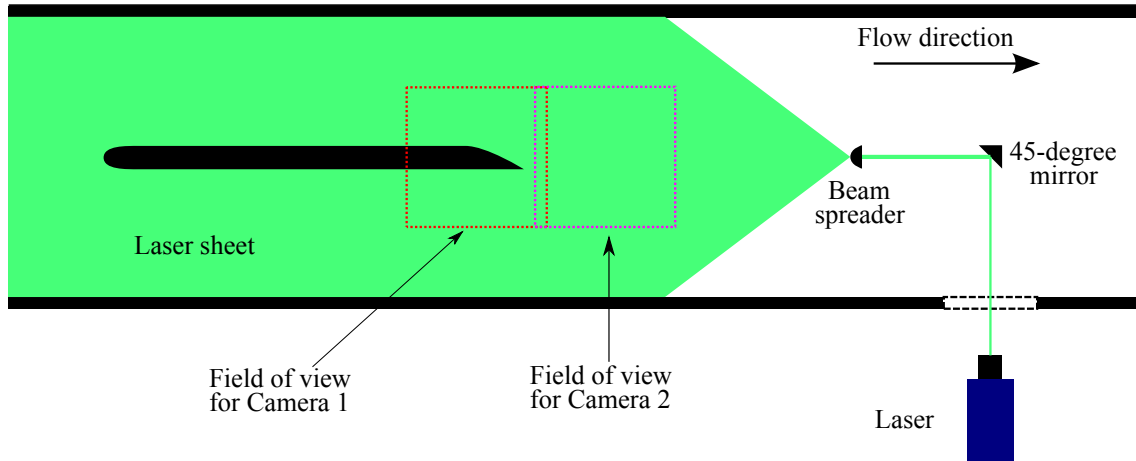


**Fig. 3** Schematic of low-repetition-rate PIV experiment on large-scale models.

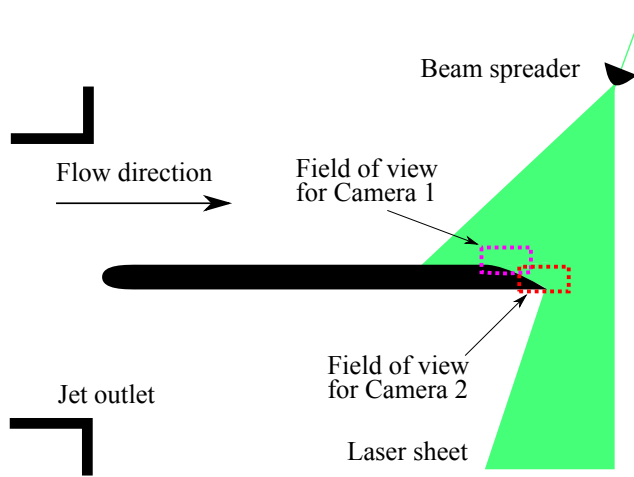


**Fig. 4** Schematic of high-speed PIV experiment on small-scale models.

the trailing edge and upper-surface boundary layer. A Quantronix Darwin Duo Nd:YLF laser ( $2 \times 25\text{mJ}$  at  $1\text{kHz}$ ) illuminated the particles through an arrangement of light-sheet forming optical elements over the FOV. The flow was seeded upstream of the settling chamber with evaporated water-glycol based fog fluid having a mean particle droplet diameter of  $1\mu\text{m}$ .

5000 image pairs were acquired at an acquisition frequency of  $f_s = 5\text{kHz}$  with a time separation equivalent to a particle displacement of approximately 15px. LaVision DaVis was used for image interrogation employing an iterative, multi-grid, multi-pass technique implementing window deformation and Gaussian window weighting with a final interrogation window size of  $16 \times 16\text{px}$ . Table 2 summarizes the parameters for the low-repetition-rate PIV experi-

**Table 2** Parameters for planar 2-component PIV on large-scale and small-scale models.

parameter	symbol	large-scale models	small-scale models
PIV method		low-repetition-rate PIV	high-speed PIV
combined field of view	FOV	$561 \times 303\text{mm}^2$	$42 \times 21\text{mm}^2$
magnification	$M$	0.06	0.49
imaging resolution		7px/mm	24.4px/mm
interrogation window size	$\delta_x \times \delta_y$	$64 \times 64\text{px}^2$	$16 \times 16\text{px}^2$
		$9.06 \times 9.06\text{mm}^2$	$0.66 \times 0.66\text{mm}^2$
		$0.18T \times 0.18T$	$0.033T \times 0.033T$
free-stream displacement	$dx$	$\sim 2.3\text{mm}$	0.62mm
	$dx/S$	$\sim 16\text{px}$	15px
acquisition frequency	$f_s$	3Hz	5kHz
number of samples	$N$	1000	5000

ments on the large-scale models and the high-speed PIV experiments on the small-scale models.

### 3 Effect of the geometry on the mean flow

#### 3.1 Mean velocity field and flow topology

Figure 5 shows the contours of the time-averaged streamwise velocity component for three representative trailing edges ( $R/T = 0, 4,$  and  $10$ ). These trailing edges are selected to represent the range of conditions. Specifically, these results illustrate a trailing edge with fixed separation point at the obtuse corner ( $R/T = 0$ ), a trailing edge with an extended adverse pressure gradient region and attached flow up to the trailing edge ( $R/T = 10$ ), and one between these two extremes ( $R/T = 4$ ). The velocity and spatial coordinates are normalized by the free-stream reference velocity  $u_\infty$  and model thickness  $T$ , respectively. For comparison the contours for the mean velocity obtained over the small-scale models (bounded by white dashed line) are overlaid over those for the large-scale models. Even though the experiments were performed within different facilities, with different models, and at different Reynolds numbers, a very good qualitative agreement is observed. The flow velocity on both sides of the model remains very close to the free-stream value since little net lift is created by the edge asymmetry. Some differences are noted and will be discussed in the following.

The  $R/T = 0$  case (Figure 5a) shows a large region of reversed flow over the beveled side of the trailing edge downstream of the separation point, which is indicated by the negative streamwise velocity component and bounded by the model surface and separated shear layers. Two separation points can be identified: on the lower side, the boundary layer remains attached up to  $x/T = 0$ . On the upper surface of the airfoil, boundary layer separation occurs upstream at the discontinuity posed by the obtuse corner ( $x/T = -2.1, y/T = 1$ ). This early separation on the upper surface results in a wake with a width approximately equal to the plate thickness ( $\sim T$ ). The results from the campaigns

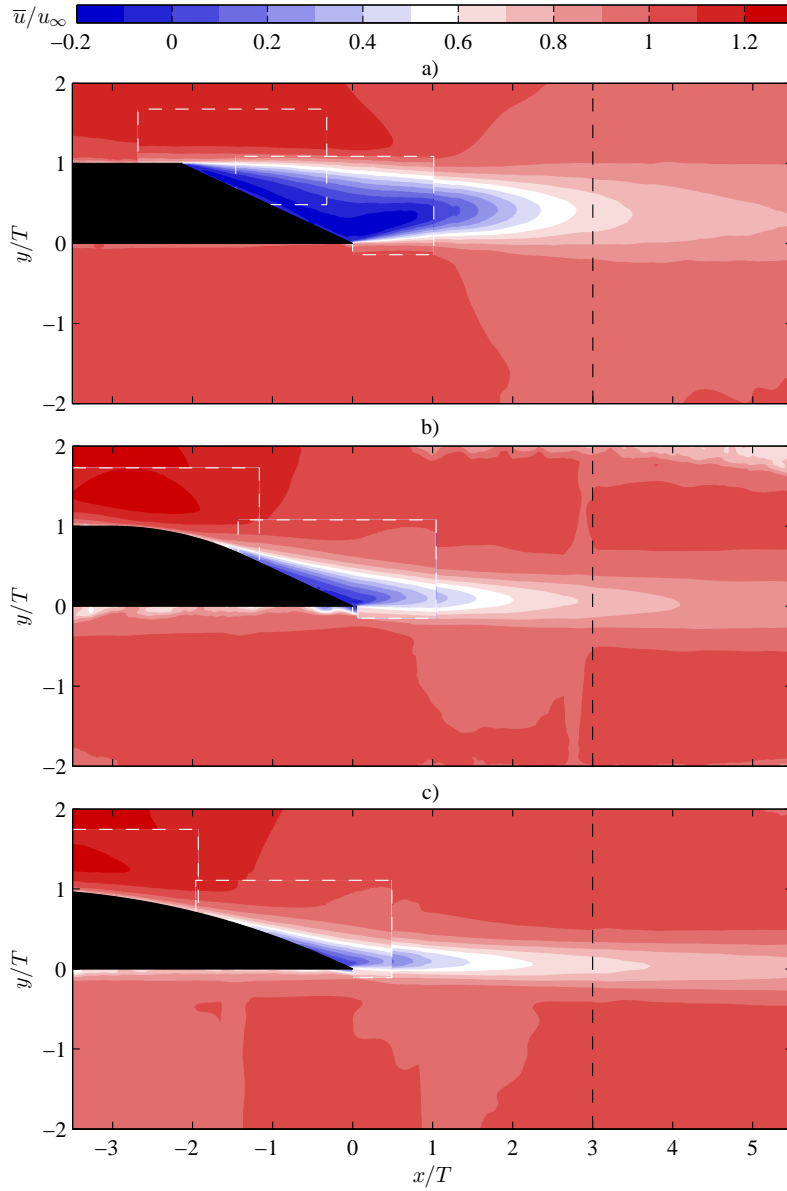


**Fig. 5** Contour levels of the mean streamwise velocity component  $\bar{u}/u_\infty$  for (a)  $R/T = 0$ , (b)  $R/T = 4$ , (c)  $R/T = 10$ . Data for small-scale models are shown within the dashed contours. The vertical, dashed line indicates integration contour used in section 3.2.

on the small- and large-scale models compare favorably in the lower half of the wake region. The spread of the upper shear layer and extent of the separated flow region was similar in both experiments. A small downward shift of approximately  $\Delta y/T \approx 0.05$  is noted for the large-scale models at  $x/T = 1$ .

For  $R/T = 4$  (Figure 5b), the results shows a significantly smaller region of reversed flow and a concomitant smaller wake when compared with  $R/T = 0$  (Figure 5a). The rounded upper surface results in an acceleration of the potential flow to a maximum velocity of approximately  $u/u_\infty \approx 1.2$  around  $x/T = -2.7$ , which has been reported earlier [Wang and Moin, 2000]. This associated favorable pressure gradient results in a very thin boundary layer in the region  $-3 < x/T < -1.5$ . Between  $-1.5 \leq x/T \leq -0.8$ , the boundary layer thickens rapidly under the influence of the severe adverse pressure gradient before separation at  $x/T \approx -1.2$ . In contrast, the turbulent boundary layer on the lower surface remains attached down to  $x/T = 0$ . In general, the two different measurements are generally in both good quantitative and quantitative agreement. At  $x/T \approx 1$ , a slight discontinuity ( $\Delta\bar{u}/u_\infty \approx 0.06$ ) is observed between the streamwise mean velocities obtained from the large- and small-scale models indicating the large-scale model creates a longer separation region in the streamwise direction. This is probably due to the higher Reynolds number of the large-scale models.

With  $R/T = 10$  (Figure 5c), the flow shows a strong acceleration of the upper surface potential flow, which extends far upstream (not in the FOV) and deceleration over the beveled part of the surface. The attached boundary layer on the upper surface thickens gradually downstream of the acceleration region under the influence of the adverse pressure gradient and attains a state close to separation at  $x/T = 0$ , which is evidenced by a small region with inflectional velocity profiles. At the Reynolds number shown here, reverse flow was not identified in the mean streamwise velocity indicating that separation did not occur in the time average. However, intermittent separation have occurred. As the flow remains attached on both sides of the airfoil, the velocity deficit in the wake of  $R/T = 10$  is smaller than those of the other cases.

### 3.2 Aerodynamic performance

The effect of the radius of curvature  $R/T$  on the separation point influences the overall aerodynamic characteristics of the airfoil. A measure for the integral effect of the trailing edge geometry is provided by the lift and drag coefficients. These aerodynamic coefficients are estimated for each of the geometries based on the time-mean velocity data using a control volume approach [van Oudheusden et al., 2007, Adrian and Westerweel, 2010]. Under the assumption of two-dimensional flow, the control volume is selected in the  $x - y$  plane. The inflow boundary was chosen far upstream and the outflow boundary was chosen downstream of the trailing edge, at a location where the streamlines are roughly parallel to the streamwise direction in order to ensure a small pressure gradient. Streamlines in the free stream are selected to complete the control volume at the top and bottom boundaries, which thus do not contribute to momentum transfer. Moreover, the contribution to the forcing from the viscous shear stress, Reynolds stresses and pressure at the boundaries of the control volume is assumed negligible. With the forementioned assump-

tions, the relevant balance for transfer of momentum consists in the difference between the upstream boundary and that in the wake, where primarily a momentum deficit is observed. The definitions and approximations of the lift and drag coefficients,  $c_l$  and  $c_d$  corresponding to the lift  $l$  and drag  $d$  per unit span, are then given by

$$c_l = \frac{2l}{\rho u_\infty^2 c} \approx \frac{2 \int_{-\infty}^{\infty} \bar{u}(y) \bar{v}(y) dy}{u_\infty^2 c} \quad (1)$$

$$c_d = \frac{2d}{\rho u_\infty^2 c} \approx \frac{2 \int_{-\infty}^{\infty} [u_\infty^2 - \bar{u}^2(y)] dy}{u_\infty^2 c} \quad (2)$$

Although the accuracy of the estimation is affected by the assumptions, the spatial resolution of the PIV, and the limited field of view, the computed lift and drag can provide trends for the effect of the trailing edge bluntness on the aerodynamic characteristics of the airfoil. For the evaluation of the aerodynamic coefficients in equations 1 and 2, the mean velocity field was sampled along the  $y$ -coordinate direction at constant  $x/T = 3$  (indicated by black dashed line in Figure 5). Figure 6 shows the resulting values of the aerodynamic force coefficients as a function of  $R/T$ . The lift coefficient (Figure 6a) increased with a roughly constant slope from  $R/T = 0$  ( $c_l \approx 0.0015$ ) to  $R/T = 8$ , where the maximum value of the lift coefficient  $c_l \approx 0.0095$  was found. With a further increase in  $R/T$ ,  $c_l$  decreased slightly to about 0.009 for  $R/T = 10$ , albeit within the uncertainty of the measurement and computation. The lift coefficients of the three trailing edge geometries discussed in section 3.1 are thus increasing for larger  $R/T$  as indicated in Figure 6a.

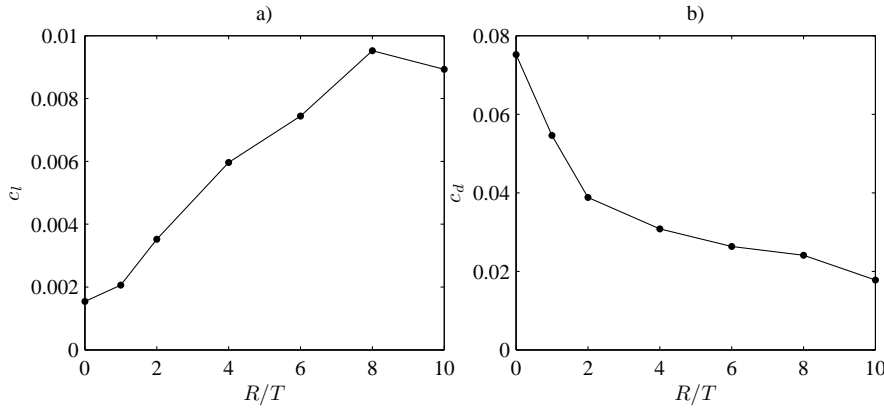


**Fig. 6** The coefficients of (a) lift  $c_l$  and (b) drag  $c_d$  for various trailing edge geometries estimated based on the PIV data acquired over the large-scale model at Notre Dame,  $Re = 1.1 \times 10^6$ .

Figure 6b shows a sharp decrease for the drag coefficient as the radius of curvature changes from  $R/T = 0$  to  $R/T = 2$ . This sharp decrease in drag

coefficient correlates with the increase in lift coefficient (Figure 6a) and is probably related to a rapid shift of the separation point to a location further downstream for geometries with radius of curvature  $R/T > 0$ . In particular, for  $R/T = 0$  the separation point is fixed at the obtuse corner on the upper surface (Figure 5), which results in a large momentum deficit in the wake. For  $R/T > 0$ , the location of the separation point is dependent on the bluntness parameter. Further decrease in bluntness ( $R/T > 2$ ) results in a smaller momentum deficit in the wake and a concomitant monotonic, albeit moderate, decrease in drag coefficient. These general trends in both lift and drag coefficient are thus consistent with expectations: a larger radius of curvature will generally delay separation resulting in an increase in lift and a decrease in drag coefficient. It is perhaps surprising, however, that the change from  $R/T = 2$  to  $R/T = 8$  resulted in a large change in lift (171%) with comparatively little effect on the drag (38%). This is because as the airfoil bluntness ( $T/R$ ) decreases, the separation of the upper-surface turbulent boundary layer occurs further downstream. The delayed flow separation on the upper surface results in significantly higher lift. Meanwhile, the vertical distance between upper- and lower-surface separation points decreases comparatively slowly, and thus the separation region shrinks slowly which results in smaller variation in drag. It is of interest to observe that as  $R/T$  changes from 2 to 8, the decrease in drag (38%) is close to the decrease in wake thickness (32%). This will be shown in Section 3.4.

### 3.3 Turbulent fluctuations and Reynolds stresses

The components of the Reynolds stress tensor facilitate quantifying the overall unsteadiness levels of the turbulent flow, whose integrated effect is responsible for the production of surface pressure fluctuations. The latter are in turn related to and can induce sound radiation and structural vibration which are of great interest in engineering application. Therefore, this section discusses the characteristics of the Reynolds normal and shear stresses in the wake of the varied trailing edge geometries.

Figure 7 shows contour levels of root-mean-square of the streamwise velocity component fluctuations  $\sqrt{u'u'}/u_\infty$  which is equivalent to the square-root of the streamwise normal component of the Reynolds stress tensor (left column) and transverse velocity component fluctuations  $\sqrt{v'v'}/u_\infty$  (right column) for the small-scale models ( $R/T = 0, 4, \text{ and } 10$ ) in the very near wake, where respectively  $u' = u - \bar{u}$  and  $v' = v - \bar{v}$ . In all cases, the values outside of the boundary layers and wake are below 0.5%, which does not indicate the true free-stream turbulence level, but is a measure for the measurement uncertainty.

For  $R/T = 0$  (Figure 7a), coherent regions of high  $\sqrt{u'u'}/u_\infty$  with local maxima along the  $y$ -coordinate direction are found to originate from both the lower and upper sharp corner. These local maxima coincide with the center location of the shear layers observed in Figure 5a, represented by regions of high mean shear  $\partial\bar{u}/\partial y$ . The magnitude of the streamwise mean velocity fluctu-

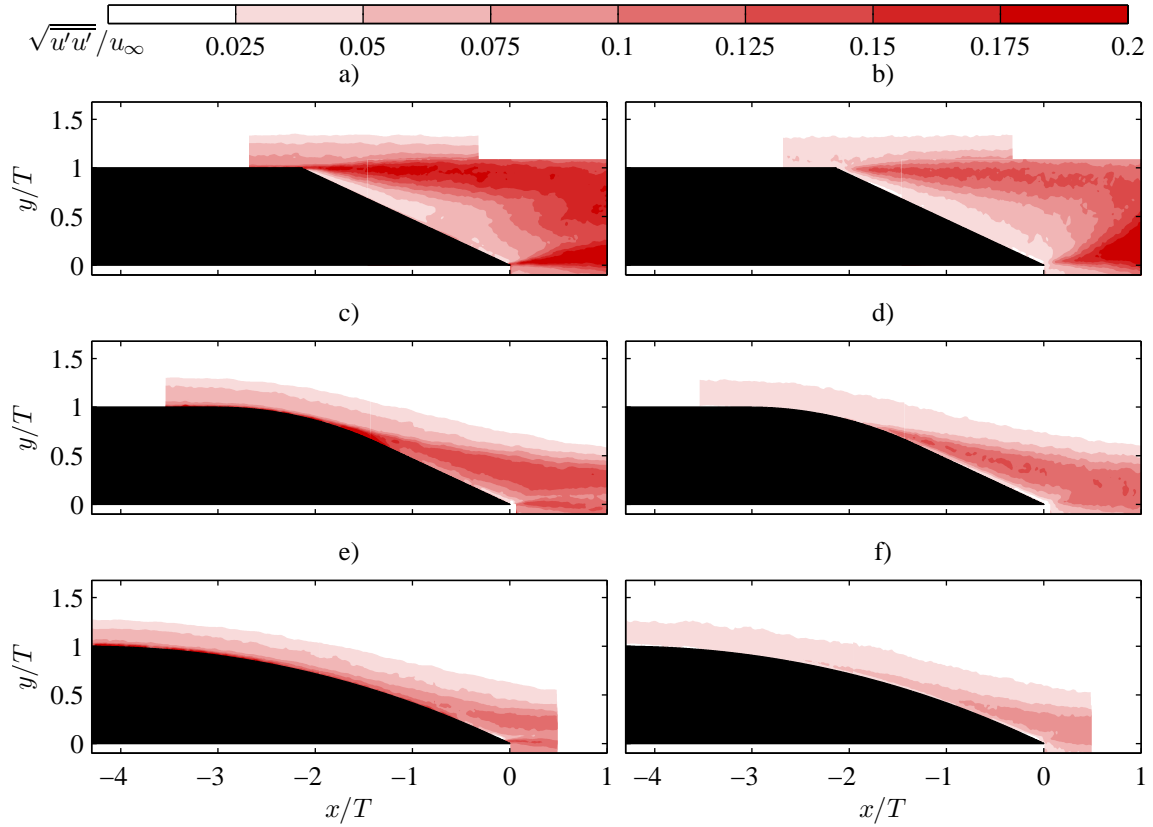


**Fig. 7** Contour levels of the streamwise ( $\sqrt{u'u'}/u_\infty$ , left column) and transverse ( $\sqrt{v'v'}/u_\infty$ , right) normal components of the Reynolds stress tensor for (a,b)  $R/T = 0$ , (c,d)  $R/T = 4$ , and (e,f)  $R/T = 10$ .

tuations reaches values of  $\sqrt{u'u'}/u_\infty \approx 0.19$  at  $x/T = -1.3$  in the upper shear layer, while it can reach 0.2 at  $x/T = 0.6$  in the lower shear layer. It should be noted that the upper shear layer develops almost parallel to the free-stream direction after the detachment and up to  $x/T = 0$ , which indicates that separation occurs and is fixed at the obtuse corner in this case. The two shear layers start to interact downstream of  $x/T \approx 0.5$  resulting in a sudden increase in the shear layer thickness. Note that within the zone of reversed flow over the upper, beveled surface the level of turbulent fluctuations is comparatively low.

For the  $R/T = 4$  case (Figure 7c), flow separation occurs further downstream near  $x/T = -1.2$  on the upper surface (Figure 5b). Thus, production of turbulent kinetic energy in the free shear layer, indicated by local maxima of  $\sqrt{u'u'}/u_\infty$ , is also observed further downstream. Related to the downstream shift of the separation point and with the flow detaching from the surface tan-

gentially, the shear layer is inclined with respect to the free stream direction at an angle of approximately  $15^\circ$ . Its thickness increases gradually downstream. A change of the inclination with adaptation closer to the free-stream flow direction is observed with transition to the wake at  $x/T \approx 0.25$ . When compared to  $R/T = 0$  (Figure 7a, left), the levels of the streamwise velocity fluctuations in both shear layers are comparatively lower. In this case,  $\sqrt{u'u'}/u_\infty$  attains a maximum of 0.15 at  $x/T = -0.1$  in the upper shear layer, which is slightly lower than that found for the  $R/T = 0$  case. This is because  $R/T=0$  results in a sharp separation at the obtuse corner and a very thin upper shear layer. The instability of the upper shear layer, coupled with the significant interaction with the opposite shear layer, results in high levels of velocity fluctuations. In contrast,  $R/T=4$  case results in a more gradual separation, and hence a thicker upper shear layer immediately after separation which produces comparatively low levels of velocity fluctuations. Note that the upper and lower shear layers remain distinct downstream, which is indicated by the local minimum of  $\sqrt{u'u'}/u_\infty$  in between.

With  $R/T = 10$  (Figure 7e), the boundary layer over the upper surface remains attached as noted in the discussion of Figure 5c. The maximum value of the turbulent streamwise fluctuations is approximately  $\sqrt{u'u'}/u_\infty = 0.11$  at  $x/T = -0.23$  in the upper shear layer and 0.13 in the lower shear layer at  $x/T = 0.07$ , and thus markedly lower when compared to the cases with smaller radius of curvature. The local maximum steamwise fluctuating components along the  $y$ -coordinate direction appears at larger wall-normal coordinates at locations downstream of  $x/T = -0.5$ , which indicates that the boundary layer on the upper surface is very close to separation although reversed flow is not observed in the time-mean results (Figure 5c).

The right column of Figure 7 shows contours of the fluctuation levels for the transverse velocity component  $\sqrt{v'v'}/u_\infty$  for the same three cases. This is often referred to as the *upwash* velocity component, and is of particular interest as the unsteady lift on the model and the radiated sound can be related to the unsteady transverse velocity component in the wake [Amiet, 1975, Howe, 1999]. For the  $R/T = 0$  case (Figure 7b), the maximum value of  $\sqrt{v'v'}/u_\infty$  in the center of the upper shear layer is 0.14. The fluctuations in the lower shear layer are largest close to  $x/T = 1$  with values in excess of 0.2, because of the interaction of the two shear layers and the formation of coherent vortex pairs. With  $R/T = 4$  (Figure 7d), the maximum upwash velocity in the upper shear layer is around 0.13, which is close to that for  $R/T = 0$ . However, the highest observed values of  $\sqrt{v'v'}/u_\infty$  over the lower surface are about 0.11, which is significantly smaller than in the  $R/T = 0$  case and probably because of the weak interaction between the shear layers. For  $R/T = 10$  (Figure 7f), both boundary layers remain attached up to the actual trailing edge ( $x/T = 0, y/T = 0$ ). The maximum  $\sqrt{v'v'}/u_\infty$  in both shear layers is approximately 0.09 and thus smaller than those in the separated cases. The smaller fluctuations in this case are attributed to the lower amplification in the attached boundary layer when compared to the free shear layer.

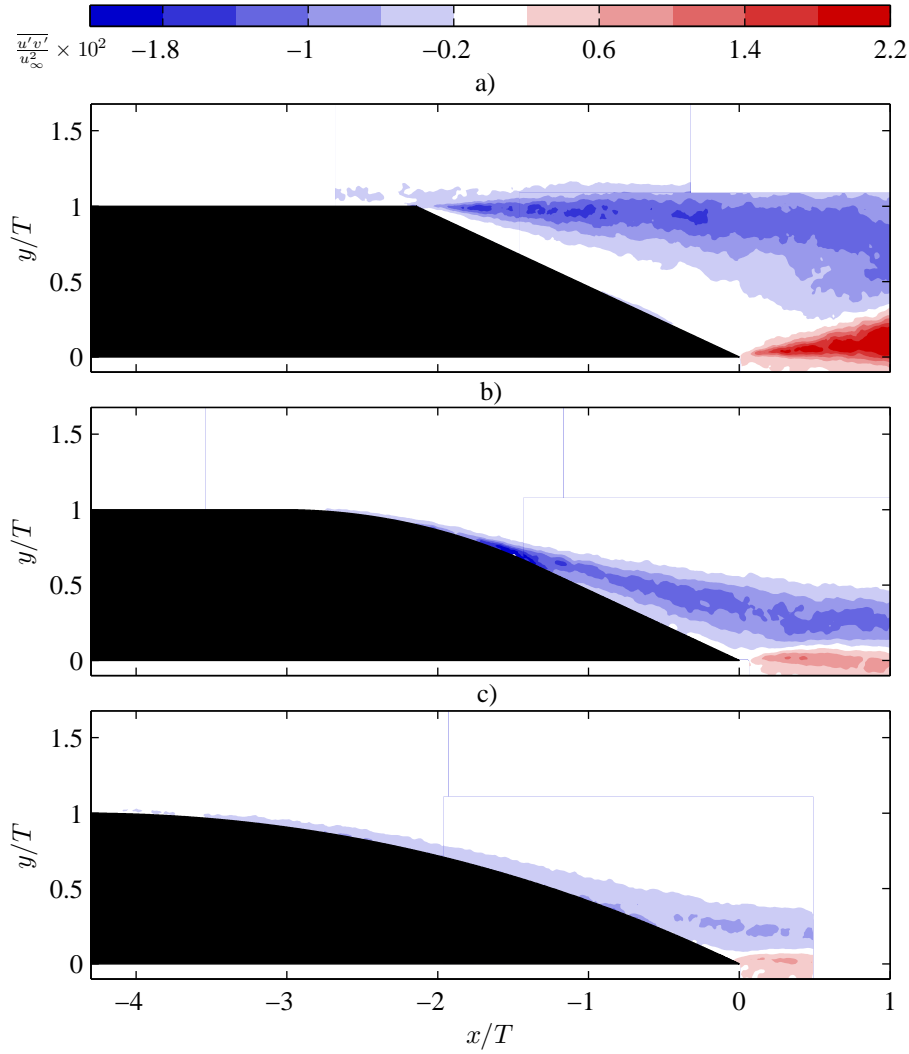


**Fig. 8** Contour levels of the Reynolds shear stress  $\overline{u'v'}/u_\infty^2$  for (a)  $R/T = 0$ , (b)  $R/T = 4$ , (c)  $R/T = 10$ .

Mohsen [1968] suggested that the local maximum Reynolds shear stress  $\overline{u'v'}_{max}$ , defined as the maximum value of the  $\overline{u'v'}$  profile along the direction normal to the solid surface, may be correlated to the large pressure fluctuations. Simpson et al. [1987] and later Na and Moin [1998] showed that scaling the wall pressure spectra using the local maximum Reynolds shear stress results in a better collapse for different streamwise locations under a separated shear layer. This procedure thus provides a more universal scaling approach. Therefore, although all Reynolds stress components are indicative of the turbulence intensity within the developing shear layer, the characteristics of the

Reynolds shear stress are of great interest. Figure 8 shows the contours of the  $\overline{u'v'}/u_\infty^2$  component of the Reynolds stress tensor. For all three cases, two regions of the shear stress are present in the near wake. The upper shear layer invokes a zone of negative shear stress, while the lower shear layer creates a more compact region of positive shear stress. For the  $R/T = 0$  case, the maximum magnitude of the positive Reynolds shear stress is approximately 50% greater than the maximum magnitude of the negative values, which is close to the ratio reported by Shannon and Morris [2006] over the  $45^\circ$  trailing edge. This indicates a strong wake asymmetry. In contrast, for  $R/T = 10$  the maximum magnitude of the shear stress in the upper and lower shear layers is similar. In general, it is noted that the magnitudes of the shear stress in both shear layers decreases monotonically with  $R/T$ , similar to the normal components in Figure 7.

### 3.4 Wake thickness parameter

Within the context of beveled trailing edges, Blake [1975] suggested the wake thickness parameter  $y_f$  as an appropriate length scale to describe the shedding of vortices into the wake. As the name suggests,  $y_f$  also serves as an indication for the thickness of the wake. The wake thickness parameter has also been defined in different context, e.g. for the shedding behind a cylinder [Tropea et al., 2007] and it should be noted that the definition is not unique. Blake [1986] defined  $y_f$  as the minimum vertical distance between the  $y$ -coordinates of the local maximum streamwise root-mean-square velocity fluctuations in the upper and lower shear layers of the near wake. This definition was employed to determine the wake length scale in a previous study of trailing edge flows [Shannon and Morris, 2006].

Based on this definition, Figure 9 shows the resulting values of  $y_f/T$  determined for the large-scale models as a function of bluntness  $R/T$ . An estimation for the uncertainty of  $y_f$  is evaluated based on the random error of the root mean square streamwise velocity  $\sqrt{\overline{u'u'}}/u_\infty$ . For  $R/T = 0$ , the value  $y_f/T \approx 0.5$  is very close to that listed by Blake [1986] ( $y_f/T \approx 0.8$ ) for  $\theta = 25^\circ$  with obtuse corner (Figure 9) taking the uncertainty into account. An increase in the radius of curvature  $R/T$  results in a monotonous decrease of  $y_f$ . The largest slope is found for small  $R/T$  and the differences become progressively smaller with increasing  $R/T$ , with the notable exception  $R/T = 10$ . For  $R/T < 10$ ,  $y_f/T$  appears to approach a value of approximately 0.25 asymptotically. Blake [1986] listed a value of  $y_f/T \approx 0.4$  for  $R/T \approx 2.5$  which shows good agreement with present results. This behavior can be understood to be related to the movement of the separation point towards the trailing edge as  $R/T$  increases. As a result, the separation point on the upper surface is associated with a lower  $y$ -coordinate. Comparing to Figure 6, it should be noted that  $y_f/T$  shows a high correlation and similar behavior to the  $c_d$  curve, which can be understood when considering that the drag is primarily related to the lower pressure over the separated flow region (pressure drag). With increasing

$R/T$  the extent of the separated flow region is reduced due to the movement of the separation point discussed above. As a result, the pressure drag decreases and so does the value of  $c_d$ . A notable difference between the behavior of  $y_f$  and  $c_d$  is the decrease in the wake thickness from  $R/T = 8$  to 10. This sudden decrease is suspected to be the result of the boundary layer remaining fully attached for  $R/T = 10$ .

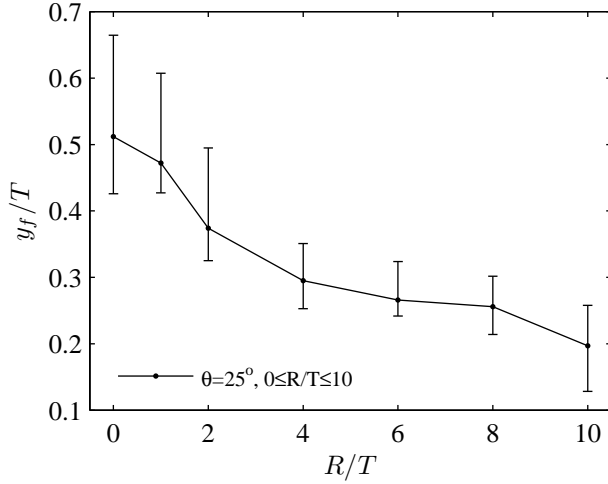


**Fig. 9** Characteristic wake thickness parameter  $y_f$  as a function of the radius of curvature  $R/T$ ,  $\text{Re} = 1.1 \times 10^6$ .

#### 4 Effect of geometry on the temporal and spatial characteristics

The mean and fluctuating velocity statistics of the near-wake flows were shown in the previous section. This section describes both the instantaneous flow field, spectra and two-point correlations of the streamwise and transverse velocity components in order to examine the spatio-temporal characteristics of the vortex shedding process and the turbulence for the various trailing edge geometries.

##### 4.1 The instantaneous flow field

Figure 10 shows contour levels of the instantaneous spanwise vorticity component  $\omega_z$ , which is normalized by the airfoil thickness  $T$  and free-stream velocity  $u_\infty$ , for the large-scale models with  $R/T = 0, 4$ , and 10. This visualization allows for examining both the small-scale vortical motion in the shear layers,

which are represented by streamwise elongated regions of concentrated vorticity, and the large-scale rotational motion in the flow field, represented by larger coherent regions of moderate vorticity.

For  $R/T = 0$  (Figure 10a), the upper free shear layer originates from the obtuse corner on the upper surface. The iso-contours of vorticity associated with this shear layer (negative values) show a wavy pattern with a wavelength of approximately  $1T$  in the streamwise direction between  $-2 < x/T < 0$ . This oscillatory and amplified motion is probably related to the instability of the free shear layer. In the region downstream of the trailing edge ( $x/T > 0.5$ ), the upper and lower shear layers start to interact through a large-scale roll-up motion, forming distinct regions of alternating positive and negative vorticity. These compact vortical structures result in a distinctive tonal character of acoustic emissions at the frequency of this vortex shedding. Notably, the wavelength associated with this large-scale vortex shedding motion is approximately  $2T$  ( $4y_f$ ) and thus about twice that of the smaller-scale oscillations in the upper shear layer. This particular near-wake structure closely resembles that reported for a beveled trailing edge ( $\theta = 45^\circ$ ) by Shannon and Morris [2006]. The large spatial separation between the two shear layers, which is due to the early separation of the upper-surface boundary layer, facilitates a very wide wake as quantified by the wake thickness parameter ( $y_f/T \approx 0.5$ ) in Figure 9. It also leads to a large distance between the vortex cores associated with the compact regions of high positive and negative vorticity in the wake.

Figure 10b ( $R/T = 4$ ) shows similar features when compared to  $R/T = 0$  (Figure 10a) with some notable differences. First, the vortex shedding is observed in the turbulent wake, but with a smaller wavelength of approximately  $1.2T$ . As for the case with  $R/T = 0$ , this wavelength corresponds to roughly  $4y_f$ , a value which is anticipated based on the results of Blake [1986], who showed the vortex shedding characteristics to scale consistently with  $y_f$ . A second, more subtle difference between the cases is the rate at which the two shear layers interact. Specifically, Figure 10a ( $R/T = 0$ ) indicates large-scale motions of alternating positive and negative vorticity for  $x/T > 0.5$ . In contrast, for  $R/T = 4$  (Figure 10b), the upper shear layer is more gradually modulated in the streamwise direction and the lower shear layer rolls up further downstream when compared with  $R/T = 0$  ( $x/T > 1.5$ ).

As Figure 5c showed, flow separation does not occur for the trailing edge with  $R/T = 10$ , although the upper surface turbulent boundary layer thickness increases significantly upstream of  $x/T = 0$  (Figure 7). In addition, Figure 10c shows that the upper and lower shear layers develop parallel to each other without strong interaction downstream of the trailing edge. A slightly wavy pattern is observed at the interface of the two shear layers downstream of the trailing edge, which is caused by the instability of the free shear layer. Significant coherent flow structures due to large-scale vortex shedding as identified for  $R/T = 0$  and 4 are not observed in the wake. Thus, the characteristics of the wake flow for  $R/T = 10$  are similar to those for sharp trailing edges [Blake, 1986].

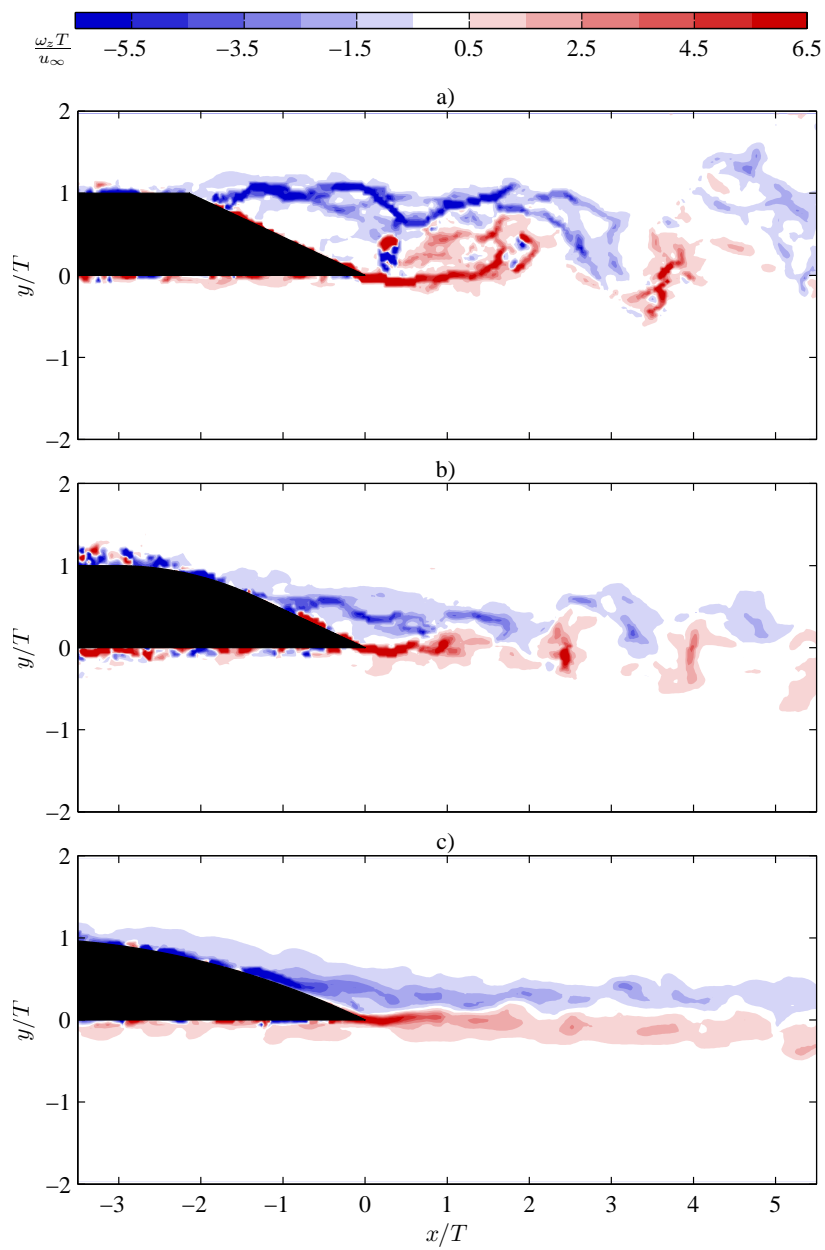


**Fig. 10** Contour levels of the instantaneous spanwise vorticity  $\omega_z T / u_\infty$  for (a)  $R/T = 0$ , (b)  $R/T = 4$ , and (c)  $R/T = 10$ .

## 4.2 Correlation of the near and far wake flow

The coherent features and structures of the wake flow observed in the instantaneous vorticity field (Figure 10) can be further analyzed using the two-point spatial correlation function of the in-plane velocity components. In particular the length scales associated with the turbulent wake are of great interest since they are important for understanding the physical nature of turbulence-induced pressure fluctuation, sound generation and structural vibration. The two-point spatial correlation coefficients of the streamwise and transverse velocity components are an indication of the average length scales associated with the coherent turbulent motions. With  $E[\cdot]$  representing the expected value, the normalized two-point velocity correlation function of two velocity components  $u_i$  and  $u_j$ , as a function of spatial locations  $\mathbf{x}_1$ ,  $\mathbf{x}_2$ , and time delay  $\tau$ , is defined by Bendat and Piersol [1986] as

$$\rho_{u_i u_j}(\mathbf{x}_1, \mathbf{x}_2, \tau) = \frac{E[u'_i(\mathbf{x}_1, t)u'_j(\mathbf{x}_2, t + \tau)]}{\sqrt{u'_i(\mathbf{x}_1)^2} \sqrt{u'_j(\mathbf{x}_2)^2}}. \quad (3)$$

Figures 11 and 12 show contour levels of the normalized two-point correlation functions with zero time delay ( $\tau = 0$ ) of the streamwise and transverse velocity components for the three trailing-edge geometries ( $R/T = 0, 4, 10$ ), respectively. In each figure, the left column shows the correlation with respect to reference points at  $x/T = 1.0$  which are chosen to be at the center location of the upper shear layer. The intent is to highlight the correlation of the boundary layer flow and the turbulent wake with velocity fluctuations in the near wake. The right column shows the correlations as calculated using reference points defined at  $x/T = 4.75$  for an indication of the correlation with velocity fluctuations in the far wake.

The wake flow for the  $R/T = 0$  (Figures 11a, b and 12a, b) shows extensive, coherent regions of alternating positive and negative correlation values for both the  $u$  and  $v$  components of velocity, which has been reported before for  $\theta = 45^\circ$  [Shannon and Morris, 2006]. Specifically, spatially alternating regions of positive and negative correlation are indicative of the spatially and temporally periodic motions which is related to the tonal character of fluctuations in the flow field at the frequency of the vortex shedding. Moreover, the correlation with the reference points in the near and far wake shows remarkable resemblance with correlation values remaining of comparable magnitude over a significant streamwise extent. This is in agreement with the large-scale vortex shedding present in the instantaneous vorticity visualization noted in Figure 10. The roll-up and interaction of the two shear layers are noted to initiate close to the actual trailing edge at  $x/T \approx 0.5$ . For locations more upstream ( $x/T < 0.5$ ), the correlation in both velocity components is significantly lower. The upper free shear layer shows weak correlation with the near-wake reference point. The very near surface regions on both sides of the model and in particular the extended region of reverse flow do not exhibit strong correlation with the near-wake or far-wake reference points.

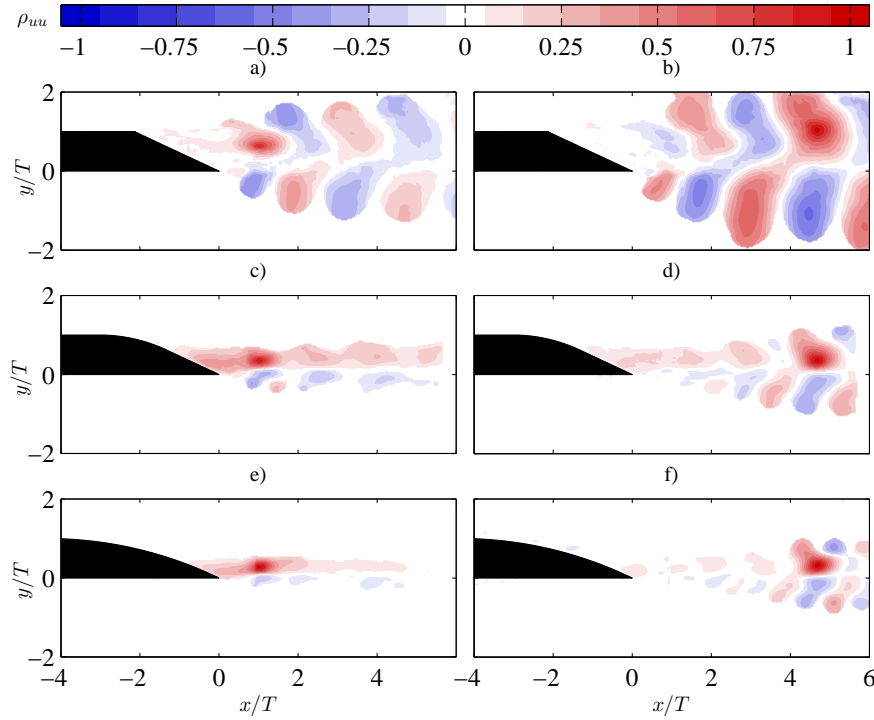


**Fig. 11** Contour levels of the two-point correlation of the streamwise velocity component  $\rho_{uu}(\mathbf{x}_1, \mathbf{x}_2, 0)$  for (a,b)  $R/T = 0$ , (c,d)  $R/T = 4$ , (e,f)  $R/T = 10$ . The coordinates  $(x/T, y/T)$  of the reference points for (a) through (f) are  $(1.0, 0.63)$ ,  $(4.7, 1.0)$ ,  $(1.0, 0.35)$ ,  $(4.7, 0.35)$ ,  $(1.0, 0.28)$ ,  $(4.7, 0.31)$ , respectively.

Interestingly, Figure 12c shows very similar features for  $R/T = 4$  when compared to  $R/T = 0$  (Figure 12a) for the transverse velocity correlations, albeit with about half the wavelength. Specifically, large alternating regions of positive and negative correlation in  $v$  appear for both the near-wake and far-wake reference locations. However, Figure 11c shows distinctive differences in the correlation of the  $u$  component when compared to  $R/T = 0$  in Figure 11a. Evidence of discrete vortex shedding in the form of alternating positive and negative correlation is not found in the near wake, but found to become more distinct further downstream ( $x/T > 2$ ) and only in the correlation with the far wake (Figure 11d). More strikingly, the  $u$  component exhibits comparatively high correlation values between either reference location and the very near-surface region on the suction side. This high correlation with the near-surface region is in contrast to the low correlation with the fluctuations in the reversed flow near-surface region for  $R/T = 0$  (Figure 11a). This is probably because for  $R/T = 4$  the separation point on the upper surface moves with the large scale oscillation of the upper shear layer, which is correlated to the turbulent wake and thus the reversed flow in the separation region shows comparatively stronger correlation with the wake.

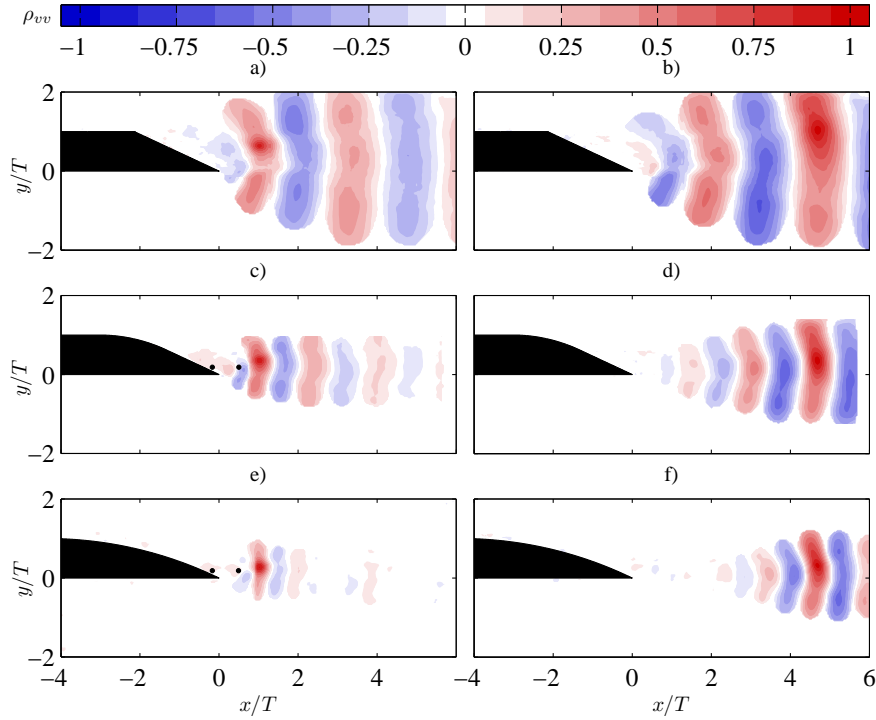


**Fig. 12** Contour levels of the two-point correlation of the upwash velocity component  $\rho_{vv}(\mathbf{x}_1, \mathbf{x}_2, 0)$  for (a,b)  $R/T = 0$ , (c,d)  $R/T = 4$ , (e,f)  $R/T = 10$ . The coordinates  $(x/T, y/T)$  of the reference points for (a) through (f) are  $(1.0, 0.63)$ ,  $(4.7, 1.0)$ ,  $(1.0, 0.35)$ ,  $(4.7, 0.35)$ ,  $(1.0, 0.28)$ ,  $(4.7, 0.31)$ , respectively. •, data point for the computation of two-point time-correlation shown in Figure 13.

The correlation results for  $R/T = 10$  in Figures 11e and 12e also indicate a significantly different flow organization with respect to  $R/T = 0$  as could be anticipated from the instantaneous vorticity field (Figure 10c). While the overall unsteadiness levels are very low for this case as noted earlier with the contours of  $\sqrt{u'u'}$  and  $\sqrt{v'v'}$  (Figure 7), similar features to the  $R/T = 4$  case are present. Notably, the high correlation of the near-surface region including the fully attached boundary layer on the upper surface with the near-wake reference point, which was also pointed out before for  $R/T = 4$ , is a distinctive feature with respect to  $R/T = 0$  (Figure 11a). However, apart from the slightly shorter wavelength of the structures in the wake of  $R/T = 10$ , a further important difference with respect to the other cases can be noted. Namely, the absolute correlation value of streamwise velocity component fluctuations with respect to the near wake (Figure 11e) decreases rapidly in downstream direction and becomes almost zero at  $x/T > 2.5$ . Interestingly, at about the same location the absolute correlation value with respect to the far-wake reference point starts to increase (Figure 11f). This indicates the decoupling of events in the near and far wake with no strong coherent roll-up in the near wake.

Thus, the alternating regions of positive and negative correlation values of  $v'$  for  $R/T = 10$  in the near wake are due to the coupled oscillations of the two shear layers as indicated by the instantaneous vorticity field (Figure 10c).

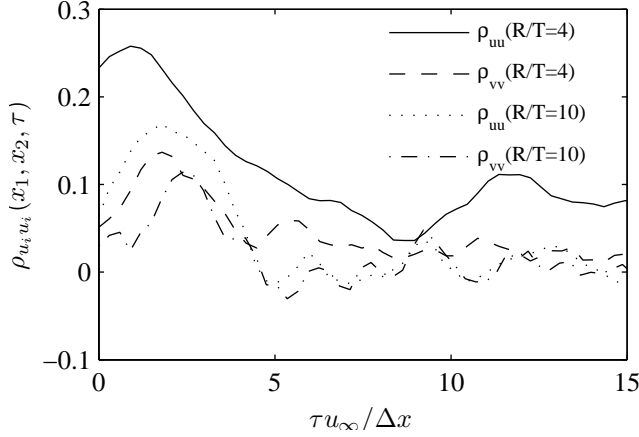


**Fig. 13** Two-point time-correlation of the streamwise and upwash velocity components for various trailing-edge geometries,  $\rho_{u_i u_i}(\mathbf{x}_1, \mathbf{x}_2, \tau)$ .  $\mathbf{x}_1$  and  $\mathbf{x}_2$  are indicated in Figure 12 by  $\bullet$ . Data were obtained from high-speed PIV measurement results.

As shown in Figure 11, the streamwise velocity fluctuation  $u'$  in the upper shear layer and the region very close to the wall correlate with the turbulent wake. The causality of the non-zero correlation between the wake and the upper-surface flow for  $R/T = 4$  and  $R/T = 10$  was investigated by observing the time-correlation of the in-plane velocity components between selected points. Figure 13 shows the normalized time correlation of the streamwise and upwash velocity components between two selected points for the various trailing edge geometries ( $R/T = 4, 10$ ). The time delay is normalized by the free-stream velocity  $u_\infty$  and streamwise spatial separation  $\Delta x$ . For  $R/T = 4$ , the two points were selected close to the upper surface in the separation region and in the turbulent wake, respectively. Similarly, for  $R/T = 10$ , the two points were selected close to the upper surface in the attached boundary layer and in the turbulent wake, respectively. The selected points are indicated in Figure 12c, e (circles).

The peak ( $\rho(\tau) \approx 0.25$ ) of the two-point time correlation of streamwise velocity fluctuation  $u'$  is found at a time delay  $\tau u_\infty / \Delta x \approx 1.5$  for  $R/T = 4$ . Although oscillation is observed, the magnitude of the time correlation decreased rapidly to below  $\rho < 0.1$  as  $\tau u_\infty / \Delta x > 5$ . The time correlation for  $R/T = 10$  exhibited similar features with respect to  $R/T = 4$  while the maximum is observed at  $\tau u_\infty / \Delta x \approx 2.1$  and its magnitude is relatively low ( $\rho(\tau) \approx 0.13$ ). The positive time delay corresponding to the maximum correlation magnitude indicates that the correlation between the velocities in the upper-surface flow and near wake is caused by the turbulent motion in the shear layer convecting

downstream. The diminishing time correlation after the presence of the peak indicates that strong coherent roll-up does not exist in the near wake. This is consistent with the observation of the two-point spatial correlation shown in Figure 12e, f. The convective velocity of the turbulent motions was computed as the ratio of the streamwise separation and the time delay associated with the maximum correlation between the selected points as  $u_c = \Delta x / \tau$ . This resulted in a convective velocity of roughly  $u_c / u_\infty \approx 0.67$  for  $R/T = 4$  and  $u_c / u_\infty \approx 0.48$  for  $R/T = 10$ . The difference is caused by the higher streamwise mean velocity of the free shear layer for  $R/T = 4$  compared to the attached boundary layer for  $R/T = 10$ .

### 4.3 Spectral energy distribution

The frequency spectra of the fluctuating velocity components indicate the distribution of turbulent energy in the frequency domain. Figure 14 shows the auto-spectral density of  $u'$  (top row) and  $v'$  (bottom row) at selected locations in the turbulent wakes. The autospectral density was estimated using the average modified periodogram method proposed by Welch [1967]. To windows with a length of 256 samples a Hamming windowing function was applied and the average was computed with an overlap of 87.5% over a total number of 149 windows, resulting in a frequency resolution of  $\Delta f = 19.5\text{Hz}$ . The frequency and velocity spectra were normalized by the free-stream velocity  $u_\infty = 20\text{m/s}$  and airfoil thickness  $T = 2\text{cm}$ . The selected locations are identified by the marker symbols in the figure.

For  $R/T = 0$ , Figures 14a and 14d show the velocity spectra at the three locations in the upper shear layer (denoted by  $\circ$  - point 1,  $\square$  - point 2, and  $\triangle$  - point 4) and one location in the lower shear layer (denoted by  $\nabla$  - point 3). The kinetic energy is comparatively high in the low frequency range ( $\log_{10}(fT/u_\infty) < -0.3$ ). For  $\log(fT/u_\infty) > -0.3$  the energy content decays, indicating that most of the kinetic energy is contributed by the low-frequency oscillations noted in Figure 10a and consistent with literature [Blake, 1975]. At locations further downstream in the upper shear layer, the low-frequency-spectral energy content increases while the high-frequency components decay further, which is attributed to the instability of the free shear layer and goes along with the development of larger-scale turbulent motions with concurring thickening of the shear layer. At any location, the amplitude of the streamwise velocity spectra (top row) is larger than that of the transverse velocity spectra (bottom row) over most part of the frequency domain keeping consistent with the results shown in Figure 7. Most notably, a marked tonal peak is observed for point 4 centered on the frequency  $\log(fT/u_\infty) \approx -0.5$  ( $\omega y_f / u_\infty \approx 1.03$ ), which is associated to vortex shedding. The tonal peak in the frequency spectra indicates that vortex shedding occurs at a constant frequency for  $R/T = 0$  [Blake, 1975]. The shedding peak is not noted in the velocity spectra in the upper shear layer at points 1 and 2, indicating that coherent vortex pairs do

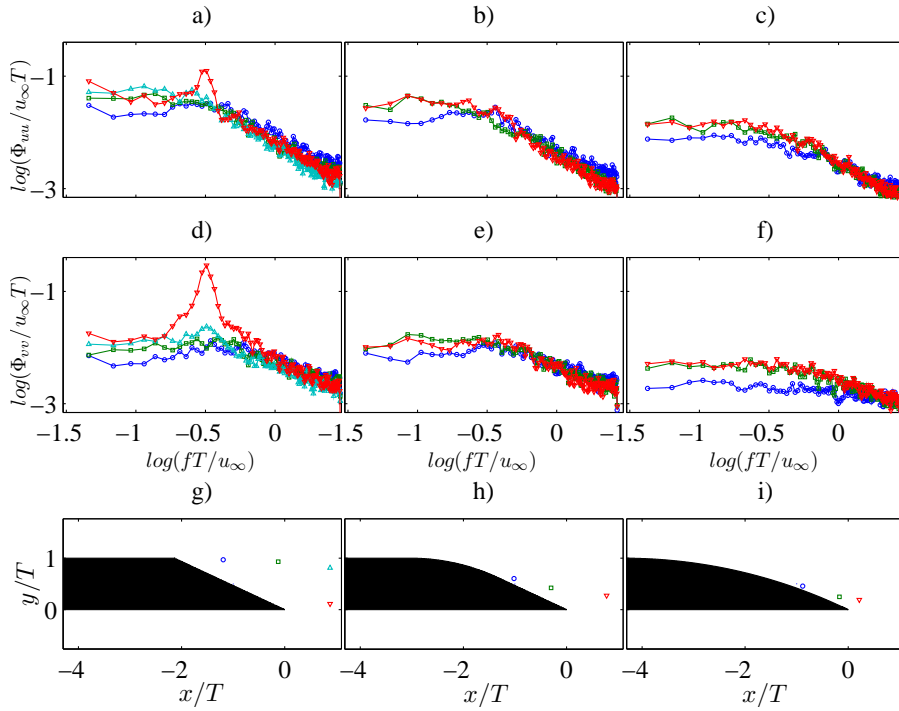


**Fig. 14** Normalized auto-spectral density of the  $u'$  (top row) and  $v'$  (bottom row) at selected locations for  $R/T = 0$  (a,d), 4 (b,e), and 10 (c,f). Data is sampled from high-speed PIV measurement results. The locations of  $\circ$  point 1,  $\square$  point 2,  $\nabla$  point 3, and  $\triangle$  point 4 are indicated in g-i.

not form upstream of  $x/T = 0.5$ , where the upper and lower shear layers start to interact and finally merge (Figure 7a).

With  $R/T = 4$  (Figures 14b), the kinetic energy is concentrated in the low frequency range ( $\log(fT/u_\infty) < -0.4$ ) and similarly to  $R/T = 0$  the spectra start to decay towards higher frequency. The low-frequency components of the velocity spectra increases at the downstream positions (point 2 and 3 compared to point 1), while the high-frequency components decreases slightly. However, when comparing the downstream positions (point 2 and 3) the kinetic energy distribution remains almost invariant. This is because the upper shear layer develops gradually to point 3 without interaction with the lower shear layer. An important difference to  $R/T = 0$  (Figure 14a) is the absence of a dominant shedding peak in the low-frequency range. The broadband low-frequency peak indicates that coherent vortex shedding is not the dominating flow feature in the near wake as already noted in the discussion of the vorticity field (Figure 10b) and also by Wang and Moin [2000].

Similar to  $R/T = 0, 4$ , the kinetic energy content for  $R/T = 10$  (Figure 14c) in the low-frequency range increases for the downstream locations in the upper shear layer (points 2 and 3 compared with point 1). It should be noted

that the overall energy, especially in the low-frequency range, is smaller than those for  $R/T = 0$  and 4, which is consistent with the lower levels of velocity fluctuations in this case as shown in Figure 7.

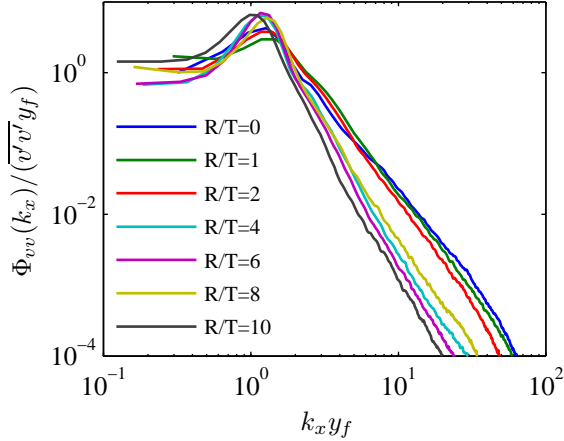


**Fig. 15** Wavenumber spectra of upwash velocity in the wake for data sampled at  $y/T = 0$  between  $0 \leq x/T \leq 6.4$ . Data are shown for large-scale models.

The final consideration of the wake flow are the wavenumber spectra of the transverse velocity component, which is closely related to unsteady lift on the airfoil and sound generation [Amiet, 1975, Howe, 1999]. The wavenumber spectrum of velocity fluctuations indicates the energy distribution over turbulent structures with various length scales. Although the trailing edge flows in the present study are not homogeneous in the streamwise direction, it is interesting to compare the wavenumber spectra of the transverse velocity component for various trailing edge geometries. Figure 15 shows the streamwise wavenumber spectra of the transverse velocity component in the wake for various trailing-edge geometries. The spectra are evaluated using an average periodogram method [Welch, 1967] applied to the data obtained on the large-scale models and sampled over a line along  $y/T = 0$  between  $0 < x/T < 6.4$ , resulting in a wavenumber resolution of  $dk_x T = 0.0991$ . The spectra obtained for each snapshot of the velocity field are averaged over 1000 frames. When the wavenumber is normalized by the wake thickness parameter  $y_f$ , a distinct maximum of the wavenumber spectrum is found for all geometries near  $k_x y_f = 1.2$  with the exception of  $R/T = 10$ . In the latter case, the maximum is found around reduced frequency ( $k_x y_f \approx 1.1$ ). This might be attributed to the upper-surface shear-layer remaining fully attached for  $R/T = 10$ , while separation of the boundary layer occurs for other cases, which results in a subtly different flow topology and thus does not follow the scaling rule found valid for the other edges. The collapse of the peak in the wavenumber spectra for the other geometries indicates that most of the kinetic energy in the wake

concentrates on turbulent structures with length scales of  $\lambda_x/y_f = 2\pi/k_x \approx 5$ . The collapse thus confirms the conclusion drawn by Blake [1986] that  $y_f$  is an appropriate length scale for the large-scale shedding in the wake flow over beveled trailing edges.

In general, as a blunter trailing edge (larger  $R/T$ ) generates a wake with larger length scale ( $y_f$ ) and higher turbulence intensity, it is more likely to produce sound with higher intensity propagating to the far-field. As shown in the spectral analysis of the velocity fluctuation in Figure 14, the low-frequency content ( $\log(fT/u_\infty) \leq -0.5$ ) of turbulent kinetic energy of the wake for blunter trailing edge ( $R/T = 4$ ) is higher than that of a sharper trailing edge ( $R/T = 10$ ). As a result, the radiated sound from the blunter trailing edge is expected to contain higher amplitude in low-frequency range. For the trailing edge with strong coherent vortex shedding in the wake, discrete tonal noise is expected at the vortex shedding frequency [Blake, 1975, Wang, 2005]. In contrast, sharper trailing edge generates sound with broadband peak [Blake, 1975, Wang and Moin, 2000].

## 5 Conclusions

The present study was focused on the measurement of the velocity field around a family of asymmetrically beveled trailing edge geometries with uniform trailing-edge angle ( $\theta = 25^\circ$ ) and various radii of curvature  $R/T$ . These measurements were made to facilitate a better understanding of the sensitivity of the flow features to changes in the design of beveled trailing edge geometries, in particular the variation in radius of curvature ( $R/T$ ). It was found that the characteristics of the trailing edge flow are highly affected by this parameter. Even subtle variation in the geometry can result in substantial changes in flow features.

The first part of the study focused on the time-mean statistics including mean velocity, aerodynamic force and Reynolds stresses. A distinct separation point exists at the upper corner of the trailing edge in the  $R/T = 0$  case, which is a distinct feature of the absence of any rounding. Strong vortex shedding with constant shedding frequency  $fT/u_\infty \approx 0.32$  is observed for  $R/T = 0$ . For larger radius of curvature (for instance  $R/T = 4$ ), the flow separates closer to the trailing edge, except for very large radius of curvature ( $R/T = 10$ ) where the flow remains attached up to the trailing edge. A smaller radius of curvature results in a larger, more turbulent wake, and has an adverse effect on the aerodynamic coefficients associated with lift and drag. Compared with the attached boundary layer, the free shear layer emanating from the upper surface in the case of separation contains higher level of turbulent kinetic energy.

The spatial and temporal characteristics of the wake flow were investigated by observing the two-point correlation, frequency spectra and wavenumber spectra of the in-plane velocity components. Coherent turbulent structures were observed in the wake of the beveled trailing edges, most notably for small radii of curvature with separation occurring further upstream. The two shear

layers interact through coherent motions a distance downstream of the trailing edge (typically  $0.5 - 1.5T$ ). These large-scale coherent motion is associated with the vortex shedding in the wake. The characteristic size of these large-scale coherent structures in the wake was proportional to the wake thickness parameter  $y_f$  (approximately  $4 - 5y_f$ ). This was further confirmed by the spatial wavenumber spectra of transverse velocity in the wake, whose peak energy content scaled on the characteristic wake thickness  $y_f$ . The upper-surface shear layer without distinct flow separation ( $R/T = 10$ ) was found to be correlated with the turbulent wake as indicated by the two-point spatial correlation. This non-zero correlation was caused by the turbulent motions convecting downstream.

**Acknowledgements** This research was supported by the U.S. Office of Naval Research (ONR), under grant numbers N00014-09-1-0050 and by the European Community's Seventh Framework Programme (FP7/2007-2013) under the AFDAR project (Advanced Flow Diagnostics for Aeronautical Research), grant agreement No.265695.

## References

- R. J. Adrian and J. Westerweel. *Particle Image Velocimetry*. Cambridge University Press, 2010.
- R. K. Amiet. Acoustic radiation from an airfoil in a turbulent stream. *Journal of Sound and Vibration*, 41(4):407–420, 1975.
- R. K. Amiet. Noise due to turbulent flow past a trailing edge. *Journal of Sound and Vibration*, 47(3):387–393, 1976.
- J. S. Bendat and A. G. Piersol. *Random Data Analysis and Measurement Procedures*. Wiley-Interscience, 1986.
- W. K. Blake. A statistical description of pressure and velocity fields at the trailing edges of a flat strut. Technical report TR-4241, David W. Taylor Naval Ship Research and Development Center, 1975.
- W. K. Blake. Trailing edge flow and aerodynamic sound. Technical report DTNSRDC-83/113, David W. Taylor Naval Ship Research and Development Center, 1984.
- W. K. Blake. *Mechanics of Flow Induced Sound and Vibration*. Academic Press, 1986.
- T. F. Brooks and T. H. Hodgson. Trailing edge noise prediction from measured surface pressures. *Journal of Sound and Vibration*, 78(1):69–117, 1981.
- W. J. Devenport, C. Muthanna, R. Ma, and S. A. L. Glegg. Two-point descriptions of wake turbulence with application to noise prediction. *AIAA Journal*, 39(12):2302–2307, 2001.
- J. E. Ffowcs Williams and L. H. Hall. Aerodynamic sound generation by turbulent flow in the vicinity of a scattering half plane. *Journal of Fluid Mechanics*, 40(4):657–670, 1970.
- J. Gershfeld, W. K. Blake, and C. W. Knisely. Trailing edge flows and aerodynamic sound. In *Proceedings of the 1st National Fluid Dynamics Conference*, pages 2133–2140, Cincinnati, USA, 1988. AIAA.

- M. S. Howe. Contributions to the theory of aerodynamic sound, with application to excess jet noise and the theory of the flute. *Journal of Fluid Mechanics*, 71(4):625–673, 1975.
- M. S. Howe. The influence of vortex shedding on the generation of sound by convected turbulence. *Journal of Fluid Mechanics*, 76(4):711–740, 1976.
- M. S. Howe. Trailing edge noise at low mach numbers. *Journal of Sound and Vibration*, 225(2):211–238, 1999.
- C. J. Knight and L. J. Peltier. Unsteady viscous simulation for beveled trailing edge flow fields. In *Proceedings of the 35th AIAA Aerospace Sciences Meeting and Exhibit*, volume 97–0662, Reno, USA, 1997. AIAA.
- C. Kunze, A. Lynch III, T. J. Mueller, and W. K. Blake. Effect of trailing edge geometry on vortex shedding and acoustic radiation. In *Proceedings of the 8th AIAA/CEAS Aeroacoustics Conference and Exhibit*, pages 2002–2435, Breckenridge, USA, 2002. AIAA.
- E. Manoha, B. Troff, and P. Sagaut. Trailing-edge noise prediction using large-eddy simulation and acoustic analogy. *AIAA Journal*, 38(4):575–583, 2000.
- A. M. Mohsen. Experimental investigation of the wall pressure fluctuations in subsonic separated flows. Technical report D6-17094, Boeing Company, 1968.
- S. C. Morris. Shear-layer instabilities: particle image velocimetry measurements and implications for acoustics. *Annual Review of Fluid Mechanics*, 43(1):529–550, 2011.
- Y. Na and P. Moin. The structure of wall-pressure fluctuations in turbulent boundary layers with adverse pressure gradient and separation. *Journal of Fluid Mechanics*, 377:347–373, 1998.
- T. Nakano, N. Fujisawa, and S. Lee. Measurement of tonal-noise characteristics and periodic flow structure around naca0018 airfoil. *Experiments in Fluids*, 40(3):482–490, 2006.
- W. Olsen and D. Boldman. Trailing edge noise data with comparison to theory. In *Proceedings of the 12th AIAA Fluid and Plasma Dynamics Conference*, volume 79–1524, Williamsburg, USA, 1979. AIAA.
- S. Olson and T. J. Mueller. An experimental study of trailing edge noise. Technical report UNDAS-IR-0105, University of Notre Dame, 2004.
- E. F. J. Overmars, N. G. W. Warncke, C. Poelma, and J. Westerweel. Bias errors in PIV: the pixel locking effect revisited. In *Proceedings of the 15th International Symposium on Applications of Laser Techniques to Fluid Mechanics*, Lisbon, Portugal, 2010.
- S. Pröbsting, A. Gupta, F. Scarano, Y. Guan, and S. C. Morris. Tomographic PIV for beveled trailing edge aeroacoustics. In *Proceedings of the 20th AIAA/CEAS Aeroacoustics Conference*, pages 2014–3301, Atlanta, USA, 2014a. AIAA.
- S. Pröbsting, J. Serpieri, and F. Scarano. Experimental investigation of aerofoil tonal noise generation. *Journal of Fluid Mechanics*, 747:656–687, 2014b.
- S. Pröbsting, M. Tuinstra, and F. Scarano. Trailing edge noise estimation by tomographic Particle Image Velocimetry. *Journal of Sound and Vibration*, 346:117–138, 2015.

- M. Raffel, C. E. Willert, S. T. Wereley, and J. Kompenhans. *Particle Image Velocimetry. A Practical Guide*. Springer, 2nd edition, 2007.
- M. Roger and S. Moreau. Broadband self-noise from loaded fan blades. *AIAA Journal*, 42(3):536–544, 2004.
- A. Roshko. On the drag and shedding frequency of two-dimensional bluff bodies. Technical report NACA TN-3169, California Institute of Technology, 1954.
- R. H. Schlinker. Airfoil trailing edge noise measurements with a directional microphone. In *Proceedings of the 4th AIAA Aeroacoustics Conference*, volume 77–1269, Atlanta, USA, 1977. AIAA.
- D. W. Shannon and S. C. Morris. Experimental investigation of a blunt trailing edge flow field with application to sound generation. *Experiments in Fluids*, 41(5):777–788, 2006.
- R. L. Simpson, M. Ghodbane, and B. E. McGrath. Surface pressure fluctuations in a separating turbulent boundary layer. *Journal of Fluid Mechanics*, 177:167–186, 1987.
- C. Tropea, A. L. Yarin, and J. F. Foss, editors. *Handbook of experimental fluid mechanics*. Springer, 2007.
- B. W. van Oudheusden, F. Scarano, E. W. M. Roosenboom, E. W. F. Casimiri, and L. J. Souverein. Evaluation of integral forces and pressure fields from planar velocimetry data for incompressible and compressible flows. *Experiments in Fluids*, 43(2):153–162, 2007.
- M. Wang. Computation of trailing-edge aeroacoustics with vortex shedding. Annual research briefs, Center for Turbulence Research, Stanford University, 2005.
- M. Wang and P. Moin. Computation of trailing-edge flow and noise using Large-Eddy Simulation. *AIAA Journal*, 38(12):2201–2209, 2000.
- P. D. Welch. The use of Fast Fourier Transform for the estimation of power spectra: A method based on time averaging over short, modified periodograms. *IEEE Transactions on Audio and Electroacoustics*, 15:70–73, 1967.